Geodesic via Asymmetric Heat Diffusion Based on Finsler Metric [*]

Fang Yang[1], Li Chai[1], Da Chen[2], and Laurent Cohen[2]

[1]Engineering Research Center of Metallurgical Automation and Measurement Technology, Wuhan University of Science and Technology, Wuhan, China
{yangfang.idif,chaili}@wust.edu.cn
[2]Université Paris Dauphine, PSL Research University, CNRS, UMR 7534, CEREMADE, 75016 Paris, France {chenda,Cohen}@ceremade.dauphine.fr

Abstract. Current image segmentation involves strongly non-uniform, anisotropic and asymmetric measures of path length, which challenges available algorithms. In order to meet these challenges, this paper applies the Finsler metric to the geodesic method based on heat diffusion. This metric is non-Riemannian, anisotropic and asymmetric, which helps the heat to flow more on the features of interest. Experiments demonstrate the feasibility of the proposed method. The experimental results show that our algorithm is of strong robustness and effectiveness. The proposed method can be applied to contour detection and tubular structure segmentation in images, such as vessel segmentation in medical images and road extraction in satellite images and so on.

Keywords: Geodesic · Minimal Path · Heat Diffusion · Finsler Metric.

1 Introduction

Geodesic refers to the shortest path connecting two points in metric space and plays an important role in image processing and computer vision. It can be applied to tasks such as contour detection, tubular structure segmentation, surface remeshing and so on [19]. In theory, the shortest path problem can be described by a static Hamilton-Jacobi equation or an anisotropic Eikonal partial differential equation (PDE). Numerical methods to compute the discrete geodesic distance on smooth surfaces and images can be classified into two classes: exact methods based on geometry and approximation method based on PDE. Generally, the approximation methods via solving the Eikonal PDE are widely used.

In terms of computation, it is difficult to get the analytical solution of the Eikonal equation directly. Therefore, an iterative relaxation scheme such as Gauss-Seidel is useful to get the numerical solution. In [13], the authors summarize popular numerical solutions to the Eikonal equation on Cartesian grids. The most popular algorithms are the Fast Marching [20] and Fast Sweeping Method [27] *etc.* By comparing the errors, speed, accuracy and robustness of different

algorithms, the authors conclude in [13] that the Fast Marching Method outperforms the other methods. However, the Fast Marching Method do not reuse its information, *i.e.*, for the same data, once the initial point is changed, the geodesic distance should be recomputed from scratch.

Recently, the geodesic method based on heat flow has become popular because of its efficiency, robustness and insensitivity to noise. It is originated from the Varadhan's formula [22]:

$$\phi(p_0, p_x) = \lim_{t \to 0} \sqrt{-4t \log u_{p_0}(p_x, t)}, \tag{1}$$

which shows that within a small time t, the geodesic distance $\phi(p_0, p_x)$ between two points p_0 and p_x can be approximated via the heat kernel $u_{p_0}(p_x, t)$.

Inspired by the classical result of Varadhan, Crane *et al.* proposed a different method for computing the geodesic distance on a Riemannian manifold, which is called the heat method [10]. Instead of using the Varadhan's formula directly, the heat method is based on solving a pair of standard linear elliptic problems.

The key observation in [10] is to divide the process of distance computation into two steps: the first step determines the direction along which the distance increases; the second step recovers the distance via solving a Poisson equation by using the normalized gradient of the heat flow. Each step relates to a standard problem in numerical linear algebra. Moreover, the sparse systems from elliptic PDEs can be solved in a very short time that is close to linear time. Therefore, the heat method can be facilitated by using existing algorithms and software, thus improves the efficiency and robustness of distance computation. In addition, for every single data, the Laplacian can be precomputed, *i.e.* recomputation is not necessary even the initial point is changed.

Though fast and efficient, the heat method described in [10] only involves the simplest case – the diffusion coefficient is a constant. To expand the scope of use of the heat method, Yang and Cohen [24] proposed to use the isotropic/anisotropic heat diffusion to obtain geodesic in images and on surfaces. In their method, the diffusion coefficient is no longer a constant, but an isotropic scalar or an anisotropic tensor computed from the image. Based on [24], the authors propose a 2D+Radius heat method for segmenting the centerline and boundary of the tubular structures simultaneously [25]. Besides, the diffusive nature of the heat equation causes instant smoothing, which is the reason why the heat method is robust to noise.

Because of the advantages of the heat method, based on Crane's work, a variety of tasks in computational science and data analysis are developed. For example, Belyaev and Fayolle [4] reinterpret the heat method and achieve more accurate results by either iterating the heat method or by applying more advanced descent strategies. Zou *et al* [28] use the heat method for efficient tool path planning; Solomon *et al* [21] use the heat method to facilitate solving optimal transport problems on geometric domains; Lin *et al* [14] apply this approach to vector-valued data in the context of manifold learning.

The heat method is popular, however, the diffusion coefficient and tensor are constructed on Riemannian manifold, which can not provide asymmetric met-

ric. While current image processing applications involve strongly non-uniform, anisotropic and asymmetric measures of path length, which can not be efficiently solved on Riemannian manifolds. Hence, in this paper, we are motivated to apply asymmetric Finsler metric to the heat method.

Finsler geometry can be described as Riemannian geometry without the quadratic restriction [9]. Riemannian distances are defined by a position dependent inner product, while Finslerian distances are defined by a direction dependent inner product, computed from a position dependent norm. Since the level sets determined by norms can be more complex than those (ellipsoidal) given by an inner product, Finsler metric is more suitable for modeling complex diffusion profiles [3].

In [15], Melonakos *et al.*proposed a Finsler active contour method by replacing the original potential in [6] into a potential including the normal of the curves. Then Zach *et al* [26] proposed a global optimal method for the Finsler active contours. Mirebeau [16] proposes an efficient discretization scheme for the Fast Marching Method on Finsler manifold. Chen *et al* [8] introduces a minimal path model with Finsler metric and uses the scheme in [16] to compute the distance. In [7], the authors extend the framework of front propagation from Riemannian manifold to Finsler manifold. The Rander's metric used in their work [7] prevents the fronts leaking problem during the fronts propagation.

The asymmetric metric is successfully applied in the Eikonal PDE, but as mentioned before, the numerical scheme Fast Marching Method is more sensitive to noise than the heat method. In addition, the Fast Marching Method do not reuse information. Therefore, we would like to develop the asymmetric heat method.

The contributions of this paper lie in that:

1. We extend the heat method based on Riemannian metric to Finsler metric;
2. We build two kinds of Rander's metric to detect contours and centerlines;
3. The asymmetric heat diffusion improves the performance comparing with the traditional heat method on image segmentation.

2   Background and Related Work

2.1   Finsler metric and minimal path model

Similar to the geodesic on Riemannian manifold, the minimal path on Finsler manifold is also obtained by minimizing the length between two fixed points. Let $\Omega \subset \mathbb{R}^N, N \in \{2,3\}$ denote the image domain, which is equipped with a Finsler metric $\mathcal{F}(x,v) > 0$, where $x \in \Omega$ denotes the position and $v \in \mathbb{R}^N$ denotes the orientation. Generally, the Finsler metric $\mathcal{F}(x,v)$ is asymmetric, *i.e.*, $\mathcal{F}(x,v) \neq \mathcal{F}(x,-v)$. The length of a Lipschitz continuous curve $\gamma(t), 0 \leq t \leq 1$ on a Finsler manifold is defined as:

$$\mathcal{L}_{\mathcal{F}}(\gamma) = \int_0^1 \mathcal{F}(\gamma(t), \gamma'(t))dt. \tag{2}$$

Note that because of the asymmetry of $\mathcal{F}(x, v)$, the curve on a Finsler manifold and its reverse curve are usually not the same.

The geodesic distance defined in (2) can be generalized to the distance from any point $p \in \Omega$ to a set of points $\mathcal{S} \subset \Omega$, thus defines the geodesic distance map:

$$\phi_{\mathcal{S}}(p) := \inf\{\mathcal{L}_{\mathcal{F}}(\gamma); \gamma(0) = p, \gamma(1) \in \mathcal{S}\}, \tag{3}$$

which is the unique viscosity solution to the following Eikonal PDE:

$$\begin{cases} \mathcal{F}^*(\nabla\phi(p)) = 1, & \forall p \in \Omega \setminus \mathcal{S}, \\ \phi(p) = 0, & \forall p \in \mathcal{S}, \end{cases} \tag{4}$$

where $\mathcal{F}^*$ is the dual metric of $\mathcal{F}$:

$$\mathcal{F}^*(x, u) = \sup_{\|v\| \neq 0} \frac{\langle u, v \rangle}{\mathcal{F}(x, v)}. \tag{5}$$

Once the geodesic distance map ϕ is obtained, the shortest path from p to $\mathcal{S}$ can be tracked by solving an ordinary differential equation (ODE) [17]:

$$\frac{\mathrm{d}\gamma(t)}{\mathrm{d}t} := \nabla\mathcal{F}^*(\nabla\phi(\gamma(t))). \tag{6}$$

In this paper, we will utilize the Rander's Finsler metric, which is defined by the combination of a symmetric Riemannian metric and an asymmetric linear part:

$$\mathcal{F}(x, v) = \|v\|_{M(x)} + \langle \omega(x), v \rangle. \tag{7}$$

According to [16], the dual to $\mathcal{F}$ is also a Rander's metric $\mathcal{F}^*$ with parameters M_* and ω_*:

$$\mathcal{F}^*(x, v) := \|v\|_{M_*(x)} + \langle \omega_*(x), v \rangle, \tag{8}$$

where M_* and ω_* are some algebraic expressions of M and ω [16]:

$$\eta := 1 - \langle \omega, M^{-1}\omega \rangle, M_* := \frac{(M^{-1}\omega)(M^{-1}\omega)^T + \eta M^{-1}}{\eta^2}, \omega_* := -\frac{M_*^{-1}M^{-1}\omega}{\eta}.$$

Hence, the backtracking ODE on the Rander's metric becomes [17]:

$$\frac{\mathrm{d}\gamma(t)}{\mathrm{d}t} = \frac{M_*(\gamma(t))\nabla\phi(\gamma(t))}{\|\nabla\phi(\gamma(t))\|_{M_*(\gamma(t))}} + \omega_*(\gamma(t)). \tag{9}$$

Compared with the Riemannian minimal path model [5], the Rander's Finsler minimal path is with an additional linear part, which is able to deal with the asymmetric information of the images.

2.2 Finsler Heat Equation

In this paper, we are dedicated to developping the heat method on the Rander's Finsler manifold. Let us consider the following energy functional:

$$\mathcal{E}(u) := \int_{\Omega} \|\epsilon \nabla u + g\|_D^2, \tag{10}$$

where D is the conductivity matrix and is positive definite by construction:

$$D = M_* - \omega_* \otimes \omega_*, \tag{11}$$

and we set $g = D^{-1}\omega_*$.

The gradient descent of (10) is interpreted as:

$$\partial_t u = \Delta_{\mathcal{F}} u, \tag{12}$$

where $\Delta_{\mathcal{F}}$ is the Finsler Laplace operator [1, 18], and (12) is called the Finsler heat equation.

Let us recall the heat method proposed in [24], where the initial condition for the heat equation is $u_{p_0}(p_x, t = 0) = \delta_{p_0}$. Therefore, the initial condition for the Finsler heat method should be the same as in [24]. The Varadhan's formula (1) presents that within a small time $t \to 0$, the heat kernel can be used to approximate geodesic distance. It is proved in [24] that the Varadhan's formula is applicable in Riemannian cases because that the geodesic distance is only related to the coefficients of the second-order derivative of the heat kernel.

In [18], the Finsler Gauss kernel $G_{\mathcal{F}^*}$ is presented by the following exponential form:

$$G_{\mathcal{F}^*}(x, t) := (4\pi t)^{-\frac{N}{2}} \exp\left(-\frac{\mathcal{F}^*(x)^2}{4t}\right). \tag{13}$$

Let $t \to 0$, put the Finsler heat kernel (13) on the *r.h.s* of the Varadhan's formula (1), according to the L'Hospital's rule, we have:

$$\lim_{t \to 0} \sqrt{-4t \log(G_{\mathcal{F}^*})} = \mathcal{F}^*(x). \tag{14}$$

Equation (14) is already well understood in the case of homogeneous heat diffusion on the whole domain $\mathbb{R}^2$, where $\mathcal{F}^*(x) = \|x\|$ and the corresponding distance is Euclidean.

3 Construction of Rander's Metric and Algorithm of the Asymmetric Heat Method

As mentioned in section 2.1, the Rander's metric is composed by a Riemannian symmetric quadratic form plus a linear part. In this section, the construction of the Rander's metric is presented. In addition, we should pay attention that in order to ensure that the metric $\mathcal{F}$ is always positive, the following constraint should be satisfied [8, 7]:

$$\langle \omega(x), M^{-1}(x)\omega(x) \rangle < 1, \forall x \in \Omega. \tag{15}$$

Different specific metrics are designed for detecting the boundaries of shapes and centerlines of tubular structures in images.

3.1 Rander's Metric for Boundary detection

In [24] and [23], the authors use either the magnitude of the gradient as the diffusion coefficient or the structure tensor to enhance the flow-like structures or edge features. Inspired by their work, we adapt these metrics to our method for detecting boundaries.

Denote by $g(x)$ the gradient of the image: $g(x) = \nabla f(x)$, where $f(\cdot)$ is a scalar function computed from the image I. The definite positive symmetric tensor field $M(x)$ can be built by the magnitude of $g(x)$:

$$M_I(x) := (\|g(x)\| + \epsilon)I_d, \tag{16}$$

where $M_I(\cdot)$ represents the tensor field in isotropic case, ϵ is a small constant that prevents the diffusion coefficient from being 0, and I_d is a 2×2 identity matrix.

$M(x)$ can be also built by the tensor product:

$$M_A(x) = \lambda_1(x)e_1(x)e_1^T(x) + \lambda_2(x)e_2(x)e_2^T(x), \tag{17}$$

where $M_A(\cdot)$ denotes the tensor field in anisotropic case, $e_1(x) = g(x)$ and $e_2(x) = g(x)^\perp$ are the eigenvectors of $M_A(x)$, $\lambda_1(x) \geq \lambda_2(x) \geq 0$ are the corresponding eigenvalues. The anisotropy A is defined as:

$$A(x) = \frac{\lambda_1(x) - \lambda_2(x)}{\lambda_1(x) + \lambda_2(x)}. \tag{18}$$

The linear part can be obtained by using the orthogonal of the normalized gradient of the image:

$$\omega(x) = \tau \left(\frac{\nabla I(x)}{\|\nabla I\|_\infty} \right)^\perp, \tag{19}$$

where τ is an adjustable coefficient which is used to satisfy (15).

Note that in [24], M_A behaves better than M_I when the feature of interest is very curved. However, in the proposed method, the difference between M_A and M_I is weakened because of $\omega(x)$.

Figure.1 shows the experimental results on a synthetic image under the same initial condition but different metrics. In (a), only (16) is used as the diffusion coefficient, without adding any additional part, which leads to a shortcut during backtracking from the endpoint to the source point. In (b) and (c), since $\omega(x)$ and $-\omega(x)$ defined in (19) are used as the linear part in the Rander's metric respectively, the heat flows more on the edge of the central black curve. Hence, during the backtracking process, the extracted curves are along the edge of the shape. Note that the closed boundary of the black central curve can be obtained by simply merging the results of (b) and (c).

Figure.1 illustrates clearly that the additional linear part $\omega(x)$ forces the heat to flow more along the direction of $\omega(x)$, *i.e.*, $\omega(x)$ enhance the heat diffusion on the edges.
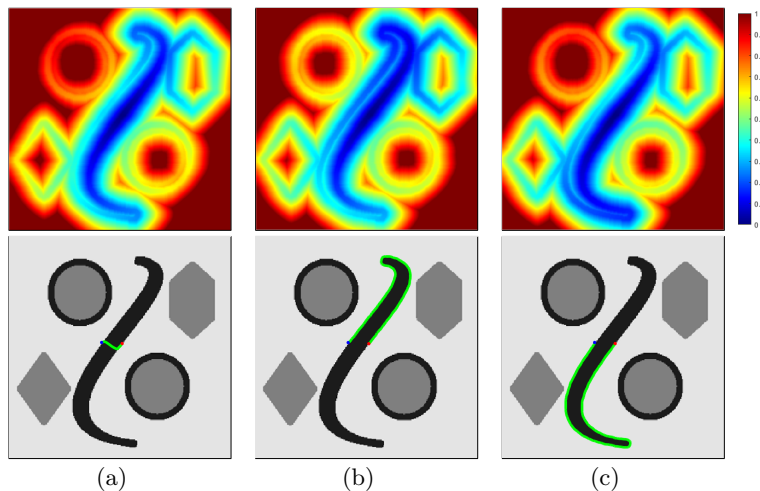
Fig. 1. From top to bottom are the distance maps and their corresponding geodesic respectively, from left to right are the results: (a) by using Riemannian metric M defined in (16), (b) by using Rander's metric whose linear part ω is defined in (19) and (c) by using the Rander's metric, the linear part $-\omega$. In the bottom row, the red and blue points denote the source point and endpoint respectively, the green curves are the geodesic curves.

Figure.2 presents an example of using different metrics on a 2D Gaussian image. First we show the Euclidean distance with the anisotropy A = 0 and its corresponding geodesic curve, which is in fact a straight line (a). In (b), we use the diffusion tensor defined in (17) as the symmetric part $M_A(x)$ with the anisotropy $A \equiv 0.9$ everywhere. We can see that the heat flows along the direction of $e_2(x)$ and the geodesic line is curved because of the anisotropic diffusion. In (c), we add the linear part $\omega(x)$. Though the geodesic curves in (b) and (c) make no difference visually, it is not hard to distinguish the distance maps from (b) and (c), which are symmetric and asymmetric respectively. In (b) the distance map is symmetric because the diffusion tensor is with quadratic form, while in (c), because of $\omega(x)$, the heat diffusion is becomes asymmetric hence flows more on the direction of $\omega(x)$. In (d), we use $-\omega(x)$ as the linear part, which is opposite to $\omega(x)$, so the heat flows in the inverse direction of (c).

The results in Fig.1 and 2 not only demonstrate the validity of the metrics designed for boundary detection, but also testify the effectiveness of the Rander's metric. In addition, both examples illustrate that $\mathcal{F}(x, v) \neq \mathcal{F}(x, -v)$.

3.2 Rander's Metric for Centerline extraction

For the purpose of extracting the centerline, the vessel enhancement method can be considered, *e.g.* Hessian-based vesselness measures [12] Here we plan to construct the symmetric part of the Rander's metric based on the eigenvalues
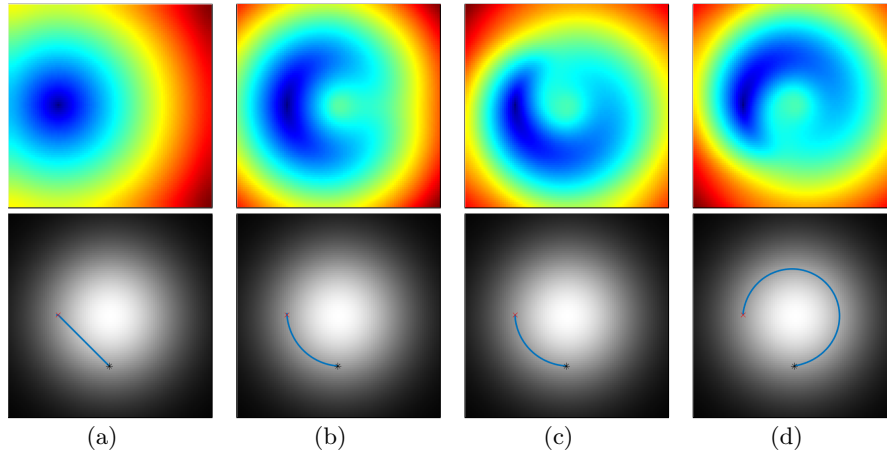
| (a) | (b) | (c) | (d) |

Fig. 2. From top to bottom are the distance maps and their corresponding geodesic respectively, from left to right are the results: (a) Euclidean, (b) using anisotropic Riemannian metric (17), (c) by using the Rander's metric with the linear part ω defined in (19) and (d) by using the Rander's metric with linear part $-\omega$. In the bottom row, the red and blue points denote the source point and endpoint respectively, the blue curves are the geodesic curves.

and eigenvectors of the Hessian matrix because of its simplicity. In [12], the authors introduced a multi-scale vessel enhancement method by interpreting geometrically the eigenvalues of the Hessian matrix. The local orientation of the image can be estimated by using the Hessian eigenvectors, which allows us to find out the position of the tubular structures.

First we convolve the image I with a Gaussian kernel $\mathcal{G}(x, \sigma)$:

$$\mathcal{G}(x, \sigma) = \frac{1}{\sqrt{(2\pi)}\sigma} \exp(-\frac{\|x\|^2}{2\sigma^2}) \tag{20}$$

Since σ can be considered as an estimator of the width of the tubular structures, we use different σ in different images. Let $I_{\mathcal{G}}$ be the product after convolution, we obtain the symmetric Hessian matrix $\mathcal{H}$ by computing the second derivative of $I_{\mathcal{G}}$:

$$\mathcal{H} = \begin{bmatrix} \partial_{xx} \ \partial_{xy} \\ \partial_{yx} \ \partial_{yy} \end{bmatrix} I_{\mathcal{G}} \tag{21}$$

Then we decompose $\mathcal{H}$ to get the corresponding eigenvectors $v_1(x), v_2(x)$ and eigenvalues $\vartheta_1(x), \vartheta_2(x)$ in order to form $M(x)$:

$$M = \vartheta_1(x)v_1(x)v_1^T(x) + \beta\vartheta_2(x)v_2(x)v_2^T(x) \tag{22}$$

where β is a constant controlled by the users to adjust the anisotropy A.

In order to prevent the heat from leaking out the region of tubular structure, we can use the eigenvector $v_1(x)$ as the linear part of the Rander's metric:

$$\omega = \tau v_1 \qquad (23)$$

where τ is an adjustable constant which plays the same role as in (19) to ensure that (15) is satisfied.

Figure.3 shows an example on a synthetic U-tube image. In this example, we set σ in (20) to be 4, β in (22) to be 0.1 and $\tau = 1$. In (a), we use the isotropic heat diffusion. The diffusion coefficient is simply obtained by using the graylevel of the image: $\alpha = (1 - (I - I_{x_0}))^n$, $n = 3$ in this case, and $M_I = \alpha I_d$. Clearly, there is a shortcut connecting the source point and the endpoint. In (b), we use the anisotropic heat diffusion where M is the diffusion tensor. The geodesic curve goes along the U tube structure this time. However, our aim is to extract the centerline of the structure. In (c), we use the Rander's metric in heat diffusion by adding ω (23). From the result, we can see that the asymmetric heat diffusion forces the heat to flow more on the main direction v_1, In the bottom row of Fig.3, although that both curves in (b) and (c) travel along the U tube structure, we can still find that the result by using asymmetric diffusion is closer to the centerline.
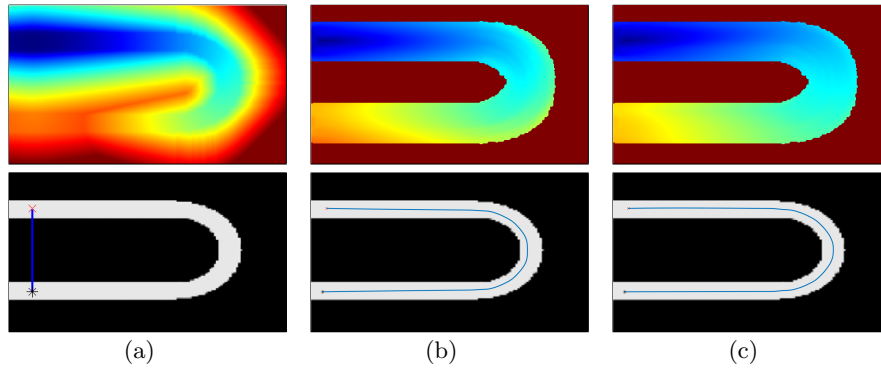

(a)   (b)   (c)

Fig. 3. From top to bottom are the distance maps and their corresponding detected geodesic curves respectively, from left to right are the results by using: (a) isotropic heat diffusion, (b) anisotropic heat diffusion with metric (17), (c) asymmetric heat diffusion with the linear part ω defined in (23).

3.3   Algorithm of the Asymmetric Heat Method

The basic steps of the asymmetric heat method can be described as follows:

In our method, the numerical solution to the Finsler heat equation and the time of diffusion (Step.2) are determined according to a backward discretization scheme designed for anisotropic heat diffusion, see [11] for details.

Algorithm 1 The Asymmetric Heat Method

---

1. Construct the asymmetric metric $\mathcal{F}(x, u)$, Sect.3.1 and Sect.3.2 ;
2. Integrate the heat flow $\partial_t u = \Delta_{\mathcal{F}} u$ from some source points for some fixed time t;
3. Approximate the distance ϕ using Varadhan's formula;
4. Backtrack the geodesic from a given endpoint to the source point using an ODE (9).

---

4   Experiments and Discussions

4.1   Experiment data and settings

We testify the effectiveness of the proposed method on both synthetic and real images. Firstly, we use a 411×411 synthetic image to testify the noise-insensitive performance of the heat method, see Fig.4. A 12% of pepper and salt noise is added to the original image. The metric is constructed by using (16) and (19), with $\tau = 1$.

For detecting the boundary of shapes in images, we choose some natural images from the BSDS500 dataset [2], see Fig.5. The gray images are used to construct metrics and initiate the heat flow.

For extracting the centerline of tubular structure, we use real road and vessel images, see Fig.6. We compare the result obtained by asymmetric diffusion with isotropic and anisotropic diffusion in [24]. For the isotropic diffusion, we preprocess the images with a sigmoid function:

$$f(x) = 1 - \frac{1}{1 + \exp(k(I - \alpha))}, \tag{24}$$

where $k = 10$ and $\alpha = 0.4$ in our tests, and $f(x)$ is used to compute the diffusion coefficient M_I in (16). For anisotropic and asymmetric diffusion, the quadratic form M_A is constructed by using (22) with a fixed $\sigma = 8$ and $\beta = 0.1$.

To display the results clearly, we use either green or blue curves to represent the extracted geodesic curve. The source points and endpoints for each image are given by the users. The red point denotes the source point and the blue ones are the endpoints.

Finally, we evaluate the quality of our algorithm on the images of BSDS500 dataset. Table.4.2 lists the recall of the detection results by symmetric diffusion method [24] and the proposed method. Note that instead of all the edges, only the geodesic curves between the two chosen points are used to calculate the recall.

4.2   Results and analysis

(1) Noisy case

In this test, the original synthetic image is corrupted by some pepper and salt noise. As we know that these kind of noise is impulse noise, it affects the image

gradient a lot. However, as we can see in Fig.4(a), most part of the extracted geodesic still goes along the edge of the center curve. Moreover, by adding the additional linear part ω and $-\omega$ (19), both geodesics travel exactly on the boundary of the curve and complete the contour of the center shape. For the result by the fast marching method (d), we use the same metric as in (b), but the result is not as good as in (b) or (c). This test demonstrates that the heat method is robust to noise, since the exponential kernel (13) causes instant smoothing.
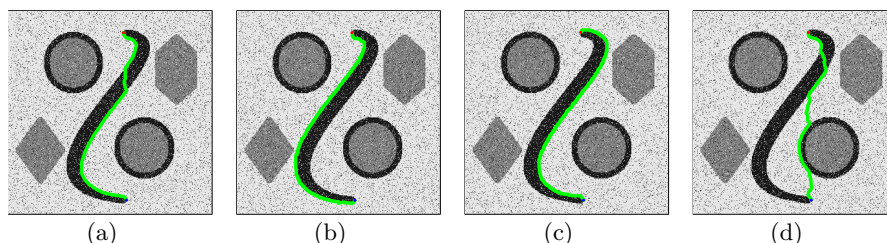

Fig. 4. Experiment on a synthetic noisy image, from left to right are the results by using: (a) isotropic heat diffusion, (b) asymmetric heat diffusion with linear part ω defined in (19), (c) asymmetric heat diffusion with the linear part $-\omega$, (d) asymmetric fast marching method (the same metric as used in (b)) .

(2) Contour Detection

The boundary and contour detection results are displayed in Fig.5. The comparison experiments are performed by using symmetric heat method in [24] with isotropic metric M_I or anisotropic metric M_A, as shown in Column.1 and Column.3 in Fig.5. The results of the proposed method are shown in Column.2 and Column.4. By using symmetric diffusion [24], the detected edges do not include some main details, *e.g.*, some elephants and the tree of *elephant*, the long pole, haystack and head of *lakeman*. As mentioned before, because of the diffusive nature of the heat kernel, the heat method can smooth the sharp changes in images, *i.e.*, noise, spurious parts. Hence in such cases, the spurious part of the edges can not be fully detected by using the symmetric heat diffusion. However, after adding the linear part ω, all the missing details are included.

Apparently, the shapes of all images are irregular and asymmetric. Because of the symmetry of the Riemannian metric, the geodesic connecting two points of using Riemmanian metric will surely be the shorter part on the contour of the shape, such as *mushroom*, *redbird* and so on. However, by adding the asymmetric linear part ω, the detected curves can go in the opposite way and thus complete the whole contour of the shape, such as *hawk*, *swan*, *mushroom* and *birds etc.* In addition, for *river*, *waterfall* and *bear*, the background is complex, therefore, the symmetric method fails to extract the edges of these shapes directly and causes some shortcuts. When adding the linear part ω, the curves are forced to go along the edges of the shapes, even the details can be detected.

The reason why asymmetric diffusion using Rander's metric works better is not only because that during the process of diffusion, the heat are more concentrated on the edges, but also on the way of backtracking, the vector field $\omega^\star$ in (9) is taken into account. However, it is worth mentioning that the proposed method to detect the boundaries are somehow sensitive to the gradient of the image, *e.g.*, the beak of the swan in Row.2, the contour of the bird in Row.5.

The quantitative results of contour detection in Fig.5 (from left to right, top to bottom) is shown in Table.4.2. Obviously, in most cases, the recall of detection results using asymmetric diffusion are higher than the symmetric ones in [24].

Table 1. Quantitative results of symmetric and asymmetric heat methods

Image	elephant	river	hawk	swan	lakeman
Symmetric recall	0.365	0.214	0.863	0.628	0.653
Asymmetric recall	0.892	0.878	0.827	0.852	0.936
Image	mushroom	redbird	waterfall	bear	bird
Symmetric recall	0.637	0.774	0.033	0.797	0.913
Asymmetric recall	0.921	0.836	0.866	0.453	0.824

(3) Centerline Detection

The results of detecting centerlines in tubular structures are shown in Fig.6. For the road image in Row.1, the curves extracted using different metrics are all smooth, despite that there is a lot of noise around the road. This example demonstrates again that the heat method is not sensitive to noise. The Column.1 of Fig.6 displays the results by using isotropic heat diffusion. As we can see, the extracted lines are not on the centerline, especially for the curved part, there is much deviation from the center. This case can be improved by using the anisotropic diffusion, which helps the heat to concentrate inside the tubular structures. However, the centerlines of the very curved parts and junctions are still not very well detected (Column.2). Finally, we combine the quadratic form with the linear part ω (23) to construct the Rander's metric. The results by using the asymmetric diffusion are shown in Column.3. Thanks to ω the extracted geodesic curves are located much more on the centerlines visually.

5   Conclusion

In this paper, we extend the traditional symmetric heat method to asymmetric cases in order to overcome the difficulty on measuring asymmetric path length. Two kinds of Rander's metric are designed for contour detection and centerline extraction. Experimental results show that asymmetric heat diffusion is effective and robust. Thanks to the asymmetric metric, the proposed method performs better than the traditional heat method. However we only consider the Rander's metric in this paper. In future, we will design different Finsler metrics to apply to the heat method according to different image processing tasks.
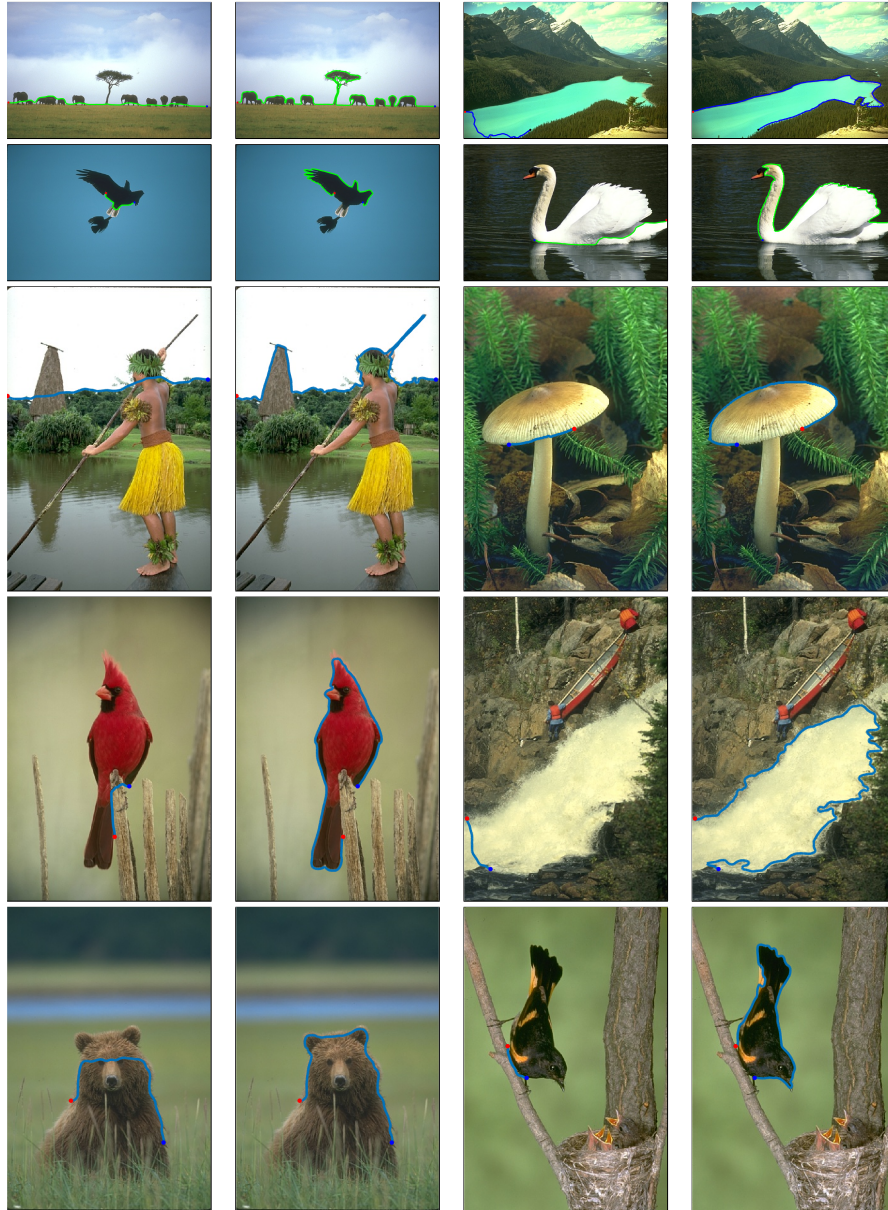
Fig. 5. Experiment on several real natural images (from left to right and top to bottom): *elephant, river, hawk, swan, lakeman, mushroom, redbird, waterfall, bear* and *bird*. The red points are the source points and the blue ones are the endpoints, the blue or green curves are the detected geodesic curves.
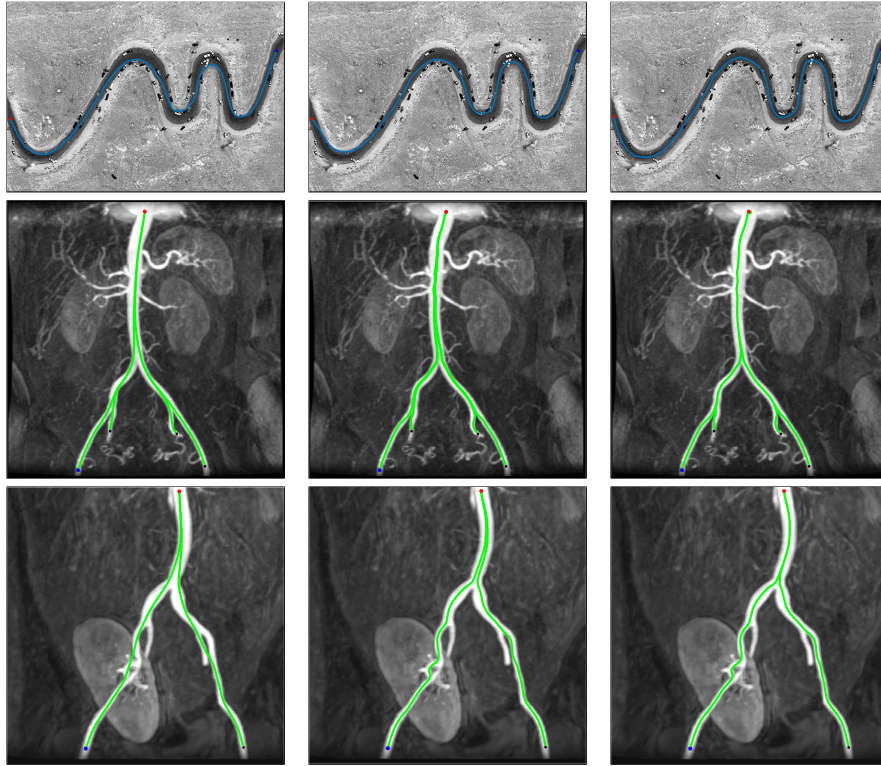
Fig. 6. Experiment on real satellite road image and vessel images, from left to right are the results by using: (a) isotropic heat diffusion, (b) anisotropic heat diffusion, (c) asymmetric heat diffusion.

Acknowledgements

References

1. Akagi, G., Ishige, K., Sato, R.: The cauchy problem for the finsler heat equation. arXiv preprint arXiv:1710.00456 (2017)
2. Arbeláez, P., Maire, M., Fowlkes, C., Malik, J.: Contour detection and hierarchical image segmentation. IEEE Transactions on Pattern Analysis & Machine Intelligence **33**(5), 898–916 (2011)
3. Astola, L., Florack, L.: Finsler geometry on higher order tensor fields and applications to high angular resolution diffusion imaging. International Journal of Computer Vision **92**(3), 325–336 (2011)

4. Belyaev, A.G., Fayolle, P.A.: On variational and pde-based distance function approximations. In: Computer Graphics Forum. vol. 34, pp. 104–118. Wiley Online Library (2015)
5. Benmansour, F., Cohen, L.D.: Tubular structure segmentation based on minimal path method and anisotropic enhancement. International Journal of Computer Vision **92**(2), 192–210 (2011)
6. Caselles, V., Kimmel, R., Sapiro, G.: Geodesic active contours. International journal of computer vision **22**(1), 61–79 (1997)
7. Chen, D., Cohen, L.D.: Fast asymmetric fronts propagation for image segmentation. Journal of Mathematical Imaging and Vision pp. 1–18 (2017)
8. Chen, D., Mirebeau, J.M., Cohen, L.D.: Global minimum for a finsler elastica minimal path approach. International Journal of Computer Vision **122**(3), 458–483 (2017)
9. Chern, S.S.: Finsler geometry is just riemannian geometry without the quadratic equation. Notices of the American Mathematical Society **43**(9), 959–963 (1996)
10. Crane, K., Weischedel, C., Wardetzky, M.: Geodesics in heat: A new approach to computing distance based on heat flow. ACM Transactions on Graphics (TOG) **32**(5), 152 (2013)
11. Fehrenbach, J., Mirebeau, J.M.: Sparse non-negative stencils for anisotropic diffusion. Journal of Mathematical Imaging & Vision **49**(1), 123–147 (2014)
12. Frangi, A.F., Niessen, W.J., Vincken, K.L., Viergever, M.A.: Multiscale vessel enhancement filtering. In: Medical Image Computing and Computer-Assisted Intervention, MICCAI 98, pp. 130–137. Springer (1998)
13. Hysing, S.R., Turek, S.: The eikonal equation: numerical efficiency vs. algorithmic complexity on quadrilateral grids. In: Proceedings of ALGORITMY. vol. 22 (2005)
14. Lin, B., Yang, J., He, X., Ye, J.: Geodesic distance function learning via heat flow on vector fields. In: International Conference on Machine Learning. pp. 145–153 (2014)
15. Melonakos, J., Pichon, E., Angenent, S., Tannenbaum, A.: Finsler active contours. IEEE Transactions on Pattern Analysis and Machine Intelligence **30**(3), 412–423 (2008)
16. Mirebeau, J.M.: Efficient fast marching with finsler metrics. Numerische mathematik **126**(3), 515–557 (2014)
17. Mirebeau, J.M.: Anisotropic fast-marching on cartesian grids using voronoi's first reduction of quadratic forms (2017)
18. Ohta, S.i., Sturm, K.T.: Heat flow on finsler manifolds. Communications on Pure and Applied Mathematics **62**(10), 1386–1433 (2009)
19. Peyré, G., Péchaud, M., Keriven, R., Cohen, L.D., et al.: Geodesic methods in computer vision and graphics. Foundations and Trends® in Computer Graphics and Vision **5**(3–4), 197–397 (2010)
20. Sethian, J.A.: A fast marching level set method for monotonically advancing fronts. Proceedings of the National Academy of Sciences of the United States of America **93**(4), 1591–1595 (1996)
21. Solomon, J., De Goes, F., Peyré, G., Cuturi, M., Butscher, A., Nguyen, A., Du, T., Guibas, L.: Convolutional wasserstein distances: Efficient optimal transportation on geometric domains. ACM Transactions on Graphics (TOG) **34**(4), 66 (2015)
22. Varadhan, S.R.S.: On the behavior of the fundamental solution of the heat equation with variable coefficients. Communications on Pure and Applied Mathematics **20**(2), 431–455 (1967)
23. Weickert, J.: Coherence-Enhancing Diffusion Filtering. Kluwer Academic Publishers (1999)

24. Yang, F., Cohen, L.D.: Geodesic distance and curves through isotropic and anisotropic heat equations on images and surfaces. Journal of Mathematical Imaging and Vision **55**(2), 210–228 (2016)
25. Yang, F., Cohen, L.D.: Tubular structure segmentation based on heat diffusion. In: International Conference on Scale Space and Variational Methods in Computer Vision. pp. 54–65. Springer (2017)
26. Zach, C., Shan, L., Niethammer, M.: Globally optimal finsler active contours. In: Joint Pattern Recognition Symposium. pp. 552–561. Springer (2009)
27. Zhao, H.: A fast sweeping method for eikonal equations. Mathematics of computation **74**(250), 603–627 (2005)
28. Zou, Q., Zhang, J., Deng, B., Zhao, J.: Iso-level tool path planning for free-form surfaces. Computer-Aided Design **53**, 117–125 (2014)